Experiments in Fluids (2024) 65:63
https://doi.org/10.1007/s00348-024-03803-2

RESEARCH ARTICLE

Calorimetric wall-shear-stress microsensors for low-speed aerodynamics

Julien Weiss[1] · **Alain Giani**[2]

Received: 27 November 2023 / Revised: 11 February 2024 / Accepted: 19 March 2024
© The Author(s) 2024

Abstract
This article describes the design, calibration, and testing of new calorimetric microsensors for the measurement of wall shear stress in low-speed aerodynamic flows. The sensors are made of three beams of platinum-plated silicon nitride suspended over a small cavity. Their range of operation and their bandwidth are of the order of ±10 Pa and 1 kHz, respectively. Results from experimental campaigns in a laminar separation bubble, a turbulent separation bubble, and on a NACA 0015 airfoil at low Reynolds number indicate a high sensitivity and an inherent capacity to measure instantaneous backflow. This demonstrates the capability of the new sensors to accurately determine the mean and fluctuating wall shear stress in laminar, transitional, and turbulent separating and reattaching flows.

1 Introduction

The experimental determination of the shear stress created by the flow of air over a solid surface is of interest to aerodynamicists for both fundamental and practical reasons. On the fundamental side, the average wall shear stress $\overline{\tau_w}$ is used to define the friction velocity $u_\tau = \sqrt{\overline{\tau_w}/\rho}$ that normalizes turbulent mean velocity profiles into the ubiquitous logarithmic law (Bailly and Comte-Bellot 2015). The fluctuating wall shear stress $\tau'_{w,std}$ is also a central parameter, being associated with the mechanism of turbulence production in wall-bounded flows (Örlü and Schlatter 2011). In nominally two-dimensional flows, the sign of the instantaneous streamwise shear stress at the wall is used to define the forward-flow fraction γ_u that characterizes the separation process of turbulent boundary layers (Simpson 1989), while for three-dimensional separation, the vector field $\overrightarrow{\tau_w}(x, z)$ is relevant (Tobak and Peake 1982). From a more practical perspective, the wall shear stress can be seen as the local signature of the flow physics in the boundary layer, being directly impacted by laminar/turbulent transition or flow separation from the surface. On air vehicles, τ_w is thus directly connected to both friction and pressure drag.

Many types of devices have been proposed over the years to measure the average and fluctuating wall shear stress on aerodynamic surfaces. The review articles by Winter (1977); Haritonidis (1989), and Fernholz et al. (1996) provide an excellent introduction to the more classical methods. These include direct mechanical balances [e.g., Meritt and Schetz (2016) for a recent example in hypersonic flows], near-wall hot-wire sensors (Sturzebecher et al. 2001), classical hot-film sensors (Comte-Bellot 2007), or oil-film interferometry [e.g., Driver (2003)]. The recent review of Örlü and Vinuesa (2020) extends the discussion to the measurement of instantaneous wall shear stress and rare backflow events, while reviewing recent additions to the literature such as micro-pillar sensors (Große and Schröder 2008) or the advent of new Micro-Electro-Mechanical-Systems (MEMS) capacitive sensors (Chandrasekharan et al. 2011). In the context of the present article, it is worth mentioning that some sensors measure the magnitude of the wall shear stress but are unable to discern flow direction (e.g., hot films or surface hot wires), a few can only capture direction but not magnitude [e.g., thermal tufts, Schwaab and Weiss (2015)], whereas others are able to capture both direction and magnitude [e.g., MEMS sensors, Pabon et al. (2018)].

If we restrict ourselves to thermal shear-stress microsensors, those can be classified into three main groups (Kuo et al. 2012): anemometric sensors, which directly measure

✉ Julien Weiss
julien.weiss@tu-berlin.de

✉ Alain Giani
alain.giani@umontpellier.fr

[1] Fachgebiet Aerodynamik, Technische Universität Berlin, 10587 Berlin, Germany

[2] IES UMR CNRS 5214, Université de Montpellier, 34095 Montpellier, France

Published online: 12 April 2024

the convective heat transfer over a heated resistance [e.g., hot wires and hot films, Comte-Bellot (2007)], time-of-flight sensors, which measure the time elapsed between the generation of a thermal pulse and its arrival on a detector [e.g., pulsed-wire probes, Castro and Haque (1987)], and calorimetric sensors, which detect the asymmetry of the temperature profile around a heated element. The main advantage of calorimetric sensors compared to their anemometric counterparts is that the former are direction sensitive, which means that they can detect the sign of the wall shear stress as well as its magnitude. Furthermore, contrary to time-of-flight sensors, calorimetric sensors provide a continuous analog signal, which is easier to acquire and process than discrete irregular samples.

Up to now, calorimetric sensors have mostly been used for mass-flow measurements in process engineering [e.g., Lammerink et al. (1993); Sabaté et al. (2004)]. Nevertheless, several researchers have relatively recently demonstrated the applicability of calorimetric microsensors for wall shear stress measurements in aerodynamic flows. De Luca et al. (2015) introduced a calorimetric sensor based on a tungsten wire and a silicon thermopile. They validated its response in a small benchtop wind tunnel up to a maximum shear stress of 0.48 Pa. Ghouila-Houri et al. (2017) developed a calorimetric sensor for the detection of flow separation based on a gold and titanium heater element flanked by two thermistors. Unsteady measurements of the wall shear stress in a region of intermittent backflow were then performed in an ONERA wind tunnel (Ghouila-Houri et al. 2019). Finally, the present authors introduced a calorimetric microsensor made of thin films of platinum deposited on a silicon nitride surface, and determined experimental calibration laws up to an average wall shear stress of 14 Pa (Weiss et al. 2017a, b).

Over the past few years, the latter calorimetric sensors were deployed in several low-speed wind tunnels for applications ranging from the detection of flow unsteadiness in turbulent separation bubbles (Mohammed-Taifour and Weiss 2021; Weiss et al. 2022), the characterization of flow structures in active separation control experiments (Steinfurth and Weiss 2022a), or the scaling of turbulent wall jets (Steinfurth and Weiss 2022b). The function principle of these sensors, as well as their most important design parameters, were described in a series of articles published in the sensors and actuators' literature (Weiss et al. 2017a, b; Giehler et al. 2022; Chamard et al. 2023).

In the present article, our main objective is to introduce the new calorimetric wall-shear-stress microsensors to the experimental fluid dynamics community. For this, we present a comprehensive overview of their design, calibration and usage in low-speed aerodynamic flows. The article is organized as follows. In Sect. 2, the principle of operation of calorimetric sensors is first introduced based on numerical simulations on a simplified geometry. This is followed by a presentation of their practical implementation for the measurement of wall shear stress in Sect. 3 and by a discussion of their static and dynamic response in Sect. 4. Application examples in a variety of low-speed, separating and reattaching flows are then presented in Sect. 5 before a final conclusion and an outlook are offered in Sect. 6. While the article specifically concerns the type of sensors introduced by the authors in Weiss et al. (2017a), much of the discussion is relevant to any other implementation of the calorimetric mode of operation for the measurement of wall shear stress on aerodynamic surfaces. Most of the results presented herein are new, although some aspects of the sensors' fabrication (Sect. 3) and signals (Sect. 5.1) were already published before. We reproduce these earlier results for clarity and completeness, and we indicate the original references in the text and the captions.

2 Principle of operation

Let us consider a thin cylindrical metallic wire, like those typically used for hot-wire anemometry. The cylinder of diameter D is maintained at a constant temperature T_H by an electronic circuitry and is cooled by an air flow of velocity U_c and temperature T_a. Figure 1 shows a sketch of such a cylinder, together with the temperature field around it for the specific case of $T_a = 293$ K, $T_H = 393$ K, $D = 5$ µm, and $U_c = 3$ m/s. The heat transfer between the cylinder and the

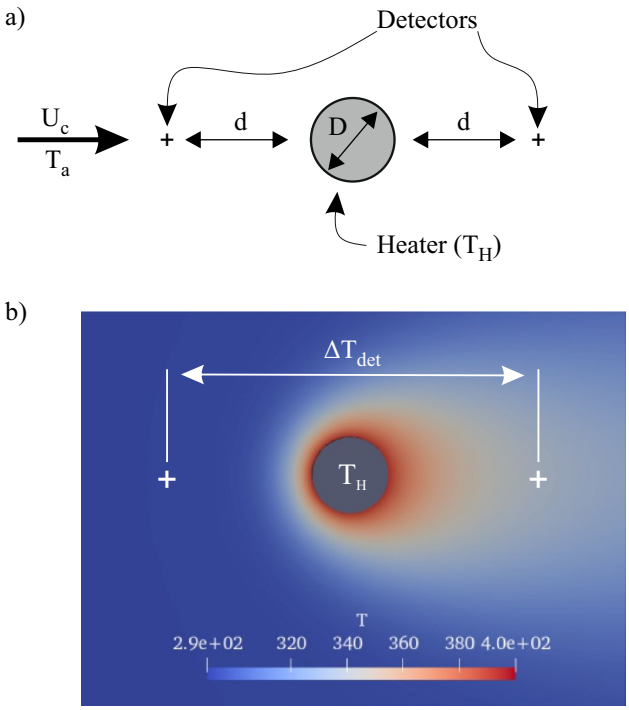

Fig. 1 Cylinder in cross flow (**a**) and associated temperature field (**b**)

air is described by the empirical law of King, which forms the basis of hot-wire anemometry (Comte-Bellot 2007). For calorimetric sensors, it is not so much the heat transfer between cylinder and fluid that is of interest, but rather the temperature field around the cylinder. To the authors' knowledge, even in the relatively simple case of a steady, two-dimensionnal, laminar flow over an infinite cylinder, there is no analytical solution to the equations of continuity, momentum, and energy that provides a temperature field $T(x, y)$ around the cylinder. Thus, in Fig. 1(b), the temperature was calculated numerically by solving those equations in their steady, laminar formulation with the OpenFOAM Computational Fluid Dynamics(CFD) software on a grid composed of 32.000 elements.

The basic concept of a calorimetric velocity sensor is to establish a relationship between the asymmetry of the temperature field around the cylinder, now called a heater, and the cooling velocity U_c (Elwenspoek and Wiegerink 2001). To achieve this, two detectors are placed at a distance $\pm d$ on the symmetry axis of the heater and the temperature difference ΔT_{det} between the right and left detectors is measured. Figure 2(a) shows examples of temperature profiles along the heater's symmetry axis for selected cooling velocities. When $U_c = 0$ m/s, the profiles on the left ($x < -D/2$) and on the right ($x > D/2$) are perfectly symmetric. In this case, only natural convection in the y direction occurs. Hence, placing a pair of detectors at any position $x = \pm d$ would lead to a temperature difference $\Delta T_{det} = 0$. On the other hand, when the cooling velocity is positive in the x-direction, the temperature profiles upstream of the cylinder are steeper than downstream because of the presence of a hot wake for $x > D/2$. Hence, in that case, ΔT_{det} is now strictly positive and may be used as a measure of U_c. Evidently, if the cooling velocity were negative ($U_c < 0$), the profiles of Fig. 2(a) would be mirrored along $x = 0$ and the temperature difference between the right and left detectors would be negative. Thus, ΔT_{det} measures the cooling velocity U_c in direction and magnitude. This is an advantage compared to classical hot-wire anemometry, where the heat transfer between the wire and the air does not distinguish between positive and negative cooling velocities.

Simple CFD simulations like those required to compute the temperature profiles in Fig. 2(a) may be used to investigate the influence of the distance d between the heater and the detectors. The temperature difference ΔT_{det} is plotted in Fig. 2(b) as a function of the cooling velocity for three selected values of d/D. These curves essentially form the calibration laws of velocity sensors that would use the calorimetric principle. Evidently, all curves are strongly non linear, with a decreasing derivative for higher values of U_c. At a certain cooling velocity, the calibration curves even reach a maximum and decrease when U_c rises further. This maximum can be clearly observed at

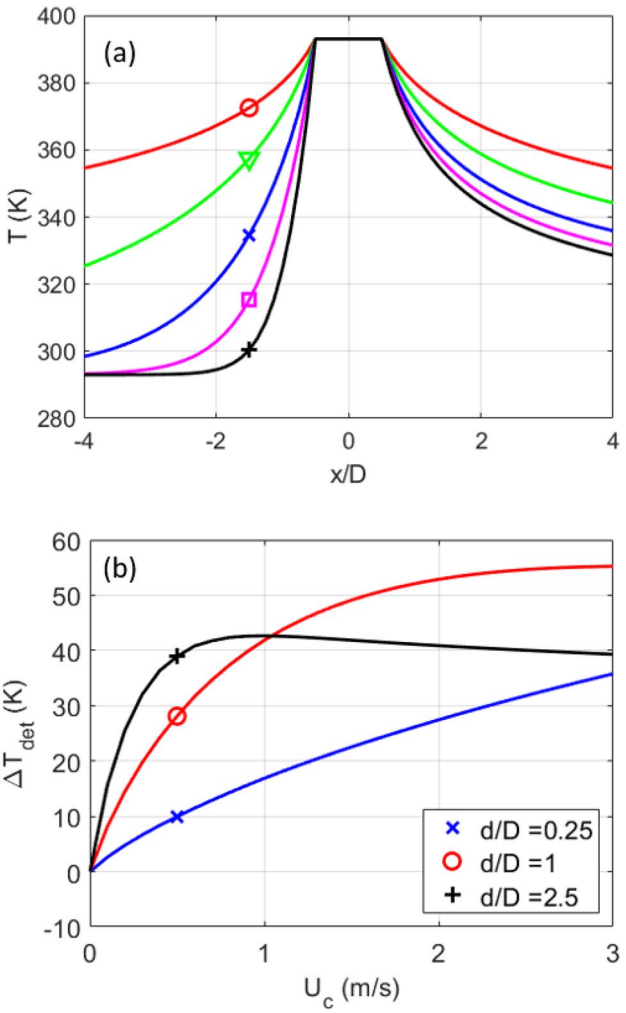

Fig. 2 Temperature profiles for $U_c = 0$ m/s (∘), $U_c = 0.1$ m/s (▽), $U_c = 0.4$ m/s (×), $U_c = 0.9$ m/s (□), and $U_c = 1.8$ m/s (+) (**a**), and associated temperature difference ΔT_{det} between two detectors placed at selected distances d/D from the heater (**b**)

$U_c \simeq 0.7$ m/s for $d/D = 2.5$. For smaller values of d/D, the maximum still exists but is out of the plotted range of velocities. Obviously, the presence of a maximum in the response curve limits the range of the instrument since any measurement above this maximum would be undetermined. Hence, calorimetric sensors are non-linear instruments with a limited measurement range (Elwenspoek and Wiegerink 2001).

The physical cause of this maximum in the response curves can be understood by looking at the temperature profiles in Fig. 2(a): when the cooling velocity increases, the temperature decreases both upstream and downstream of the heater. However, the decrease in temperature downstream is less severe than upstream because of the presence of the wake. This asymmetry forms the basis of calorimetric sensors. At a given distance d, when the cooling velocity

is high enough, the temperature upstream of the cylinder will eventually reach the fluid temperature T_a and won't decrease any further. On the downstream side, however, the temperature is still higher than T_a and continues to decline due to the mixing of cold air in the wake. Any further increase in velocity won't influence the upstream side of the heater anymore, whereas the temperature on the downstream side will continue to decline when U_c increases. At this stage the asymmetry is reversed and the maximum is attained. Based on the plots of Fig. 2(b), it is easy to see that a decrease in d/D augments the velocity at which the maximum is reached. Thus, building a calorimetric sensor with a wide measurement range requires a small distance between the heater and the detectors (Weiss et al. 2017a).

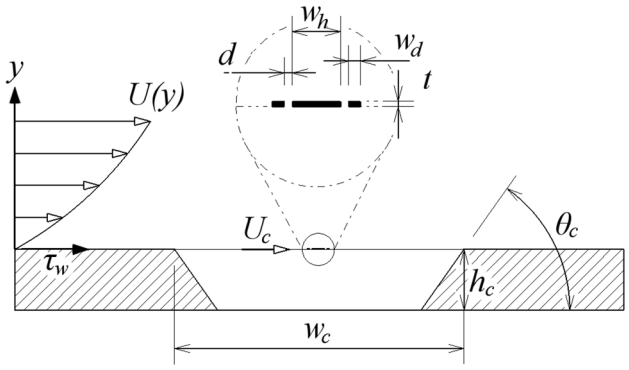

Fig. 3 Sketch of the MEMS calorimetric sensor (side view). From Weiss et al. (2017a)., reproduced with permission

3 Practical implementation

The measurement principle described in the previous section is that of a calorimetric velocity sensor. In aerodynamic applications, such a sensor would not be very useful because the fixed detectors would limit the measurement to one axis only. Nevertheless, this type of sensor is commonly used in mass-flow meters where the bulk velocity is one dimensional [e.g., Lammerink et al. (1993)]. To convert such a sensor to the measurement of skin friction, the most straightforward approach would be to replace the hot wire by a hot film placed on the surface. Measuring the difference in wall temperature upstream and downstream of the hot film would, using an appropriate calibration law, allow the detection of τ_w along the sensor axis. Hovewer, the bandwidth of such a sensor would be severely limited by heat conduction through the substrate, a problem that is well known in thermal anemometry (Sheplak et al. 1996; Chamard et al. 2023). To circumvent this issue, the approach suggested by the authors is to suspend the hot wire over a small cavity, in a manner reminiscent of the 'surface hot wire' of Sturzebecher et al. (2001).

The proposed sensor geometry is sketched in Fig. 3. Three beams are suspended over a cavity: the middle beam, called the heater, plays the role of the heated cylinder, while the two side beams are the detectors. Steady CFD simulations by Giehler et al. (2022), some results of which are reproduced in Fig. 4, show that the presence of the cavity slightly deflects the streamlines of the incoming flow and may generate a recirculating region under the beams. Hence, the cooling velocity U_c felt by the three beams is of the order of the friction velocity $u_\tau = \sqrt{\tau_w/\rho}$ just upstream of the cavity. Assuming that the cavity and beams are small compared to the overall dimensions of the test surface, the temperature difference ΔT_{det} is therefore a measure of the wall shear stress τ_w.

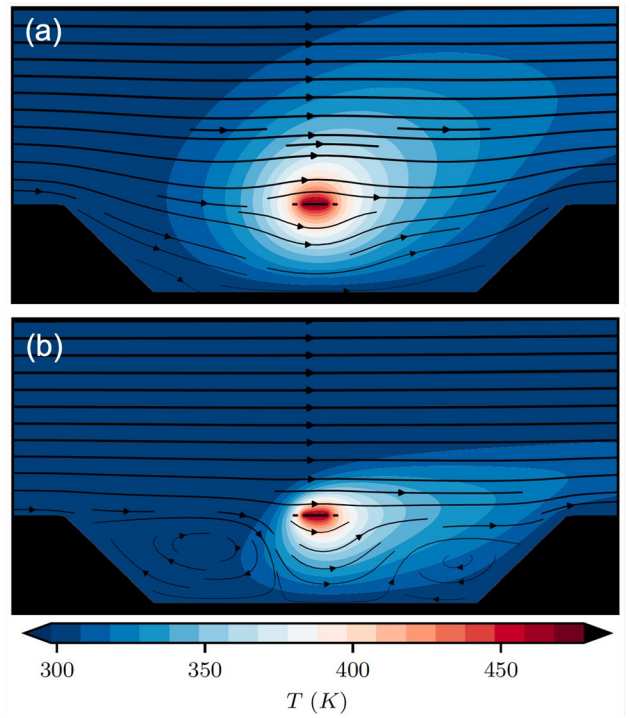

Fig. 4 Streamlines and temperature distributions near the cavity for $\tau_w = 0.1$ Pa (**a**) $\tau_w = 2.5$ Pa (**b**). From Giehler et al. (2022), reproduced with permission

The sensor is manufactured using classical micro-fabrication techniques previously developed for thermal accelerometers (Mailly et al. 2003) and described in details by Chamard et al. (2023). Briefly, the heater and detectors are made of thin films of platinum deposited on a silicon nitride membrane (SiNx), while the cavity is dug into the silicon substrate. Typical dimensions are $w_h = 25\,\mu$m for the heater width, $w_d = 5\,\mu$m for the detectors width, and $d = 5\,\mu$m for the inter-beam distance between heater and detectors. The thickness of the beams (SiNx + Pt) is $t = 0.7\,\mu$m, and their

length (across the page in Fig. 3) is $l = 1$ mm. The depth of the cavity is typically $h_c \simeq 200\,\mu$m and its footprint is 1 mm × 1 mm. The cavity angle $\theta_c = 54.7°$ is fixed by its manufacturing through KOH wet etching (Chamard et al. 2023).

Scanning electron microscope (SEM) images of two sensors are shown in Fig. 5. In the the so-called straight design (a), the beams are arranged parallel to two sides of the square cavity, whereas in the 45° design (b), the beams are suspended over the diagonal of the cavity. The latter design simplifies the manufacturing process for different cavity heights because it enables the proper removal of the silicon below the beams. Comparative studies by Chamard (2022) did not reveal any significant differences in the static and dynamic response of both types of sensors, so that they were used intergangeably in the applications that will be described in Sect. 5. In Fig. 5(c), a zoom on the three beams reveals one of the 3 support bridges that mechanically link the heater and the detectors. Those are built in the SiNx membrane to increase the structural resistance of the three-beam system (Weiss et al. 2017b).

In the current implementation, the sensor is positioned at the center of a circular PCB and connected to it by aluminum bonding wires (Fig. 6). Further connections to the electronic equipment are located on the backside of the PCB, thus enabling the arrangement to be flush mounted on a flat test surface. An obvious future technological development will be the replacement of the bonding wires by vias through the silicon substrate.

In operation, the sensors are connected to a custom-built analog electronic equipment that consists of a constant-temperature anemometer (CTA) circuit to power the heater, and a low-current Wheatstone bridge for the detectors. The output voltage E_{det} is proportional to the difference in electrical resistance between the two detectors, and thus a measure of ΔT_{det} and ultimately τ_w.

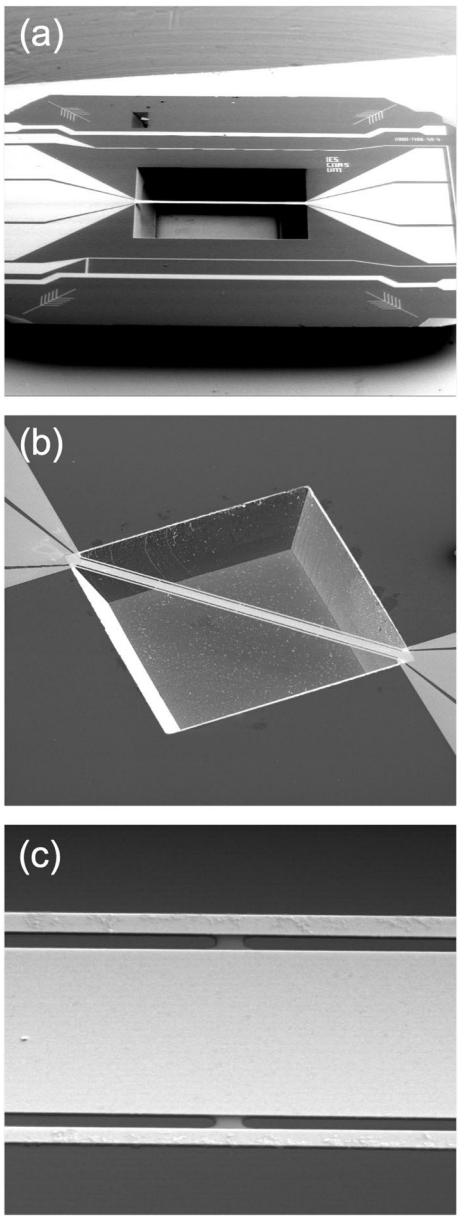

Fig. 5 SEM image of calorimetric shear-stress sensors: straight design (**a**), '45°' design (**b**), and zoom on the support bridges (**c**)

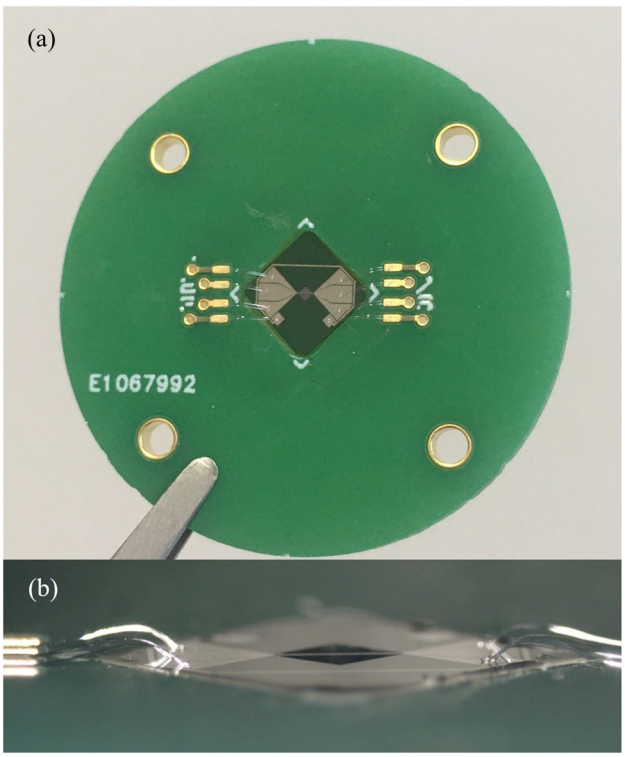

Fig. 6 Sensor packaging: circular PCB (**a**); close up on the sensor and bonding wires (**b**). Reproduced from Chamard et al. (2023) with permission

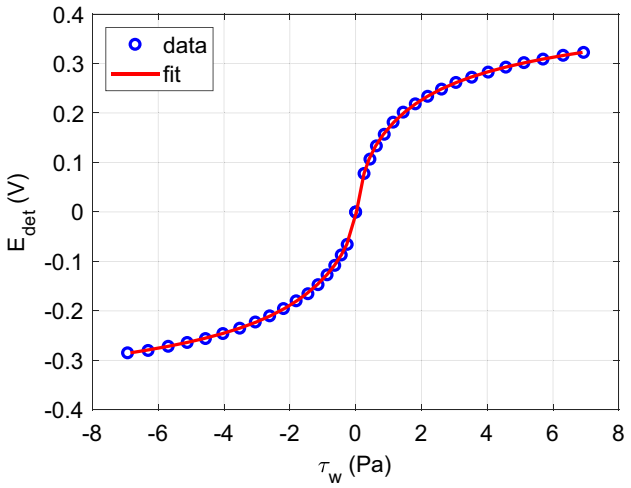

Fig. 7 Typical calibration curve of calorimetric shear stress sensor ($d = 5\,\mu$m)

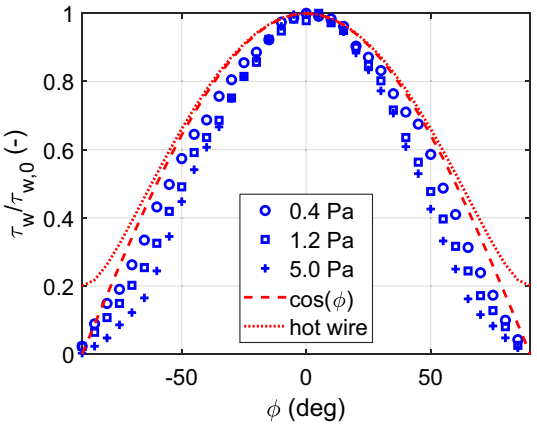

Fig. 8 Typical angular calibration of calorimetric shear stress sensor. Values in the legend indicate the nominal wall shear stress $\tau_{w,0}$ at $\phi = 0°$

4 Calibration

An example of static calibration curve $E_{\text{det}} = f(\tau_w)$ is shown in Fig. 7. The data points represented as circles were obtained in a rectangular channel flow serving as calibration facility where τ_w is set by imposing the longitudinal pressure drop. The calibration curve is a 7^{th}-order polynomial fit that has the general form of the plots shown in Fig. 2. A close inspection reveals that the calibration curve is not perfectly anti-symmetric, which is attributed to small geometrical imperfections of either the sensor or its mounting on the PCB. This particular sensor has an inter-beam distance $d = 5\,\mu$m and its range is larger than ± 8 Pa. In fact, measurements up to $\tau_w = 14$ Pa were already performed with similar sensors, whereas sensors with $d = 10\,\mu$m reached their maximum at $\tau_w \simeq 7$ Pa (Weiss et al. 2017b). Once a calibration curve such as Fig. 7 is obtained, measurements of τ_w on an aerodynamic surface may be performed by recording E_{det}.

Angular calibrations were also performed in the same channel flow facility with several sensor prototypes. The variation of the measured value of τ_w as a function of the sensor angle ϕ with respect to the main flow direction is shown exemplarily in Fig. 8 for three values of the nominal wall shear stress $\tau_{w,0}$. Here, we define $\phi = 0°$ when the incoming flow is exacly perpendicular to the sensing beams. This particular sensor had a 45°-design with an inter-beam distance of $d = 5\,\mu$m. Different sensors produced very similar, though non identical responses. Also shown in the figure is the cosine law that would ideally be obtained for an infinitely long hot wire (dashed line) and a more realistic hot-wire angular response $(\cos^2(\phi) + k^2\sin^2(\phi))^{1/2}$ (dotted line), where $k = 0.2$ is the yaw factor for a typical length-to-diameter ratio of 200 (Champagne et al. 1967; Bruun 1995).

For all values of the angle ϕ outside of a small $\pm 10°$ range, the measured $\tau_w/\tau_{w,0}$ lies below the cosine law. This is contrary to typical hot wires, where the angular calibration curves are usually slightly above the cosine law due to tangential cooling along the wire (i.e., $k > 0$). The latter effect is particularly obvious near $\phi = \pm 90$ deg, where most of the cooling occurs along the wire. In contrast, all measured values of $\tau_w/\tau_{w,0}$ for the calorimetric sensor tend to zero for $\phi = \pm 90°$, which is expected given its differential method of operation. Indeed, as already shown in Fig. 7, calorimetric sensors are direction sensitive, so that the sign of their output voltage E_{det} changes when ϕ crosses the $\pm 90°$ lines. Furthermore, for the calorimetric sensor, the deviation from the cosine law depends on the nominal wall shear stress $\tau_{w,0}$. This effect is attributed to the presence of the square cavity under the sensing beams, which likely affects the velocity field near the detectors as a function of the inflow angle and magnitude. Clearly, based on the data presented in Fig. 8, accurate measurement of the wall shear stress with a calorimetric sensor inclined more than $\pm 10°$ with respect to the mean flow direction requires a comprehensive angular calibration in addition to the longitudinal calibration presented in Fig. 7.

In addition to being sensitive to the local velocity near the wall, calorimetric sensors, like other thermal sensors, are also sensitive to the air temperature T_{a}. Hence, if a sensor is calibrated against the wall shear stress at a reference temperature T_{ref} that differs from the temperature T_{a} occuring during the measurements, a correction of the measured voltage will be necessary. This effect is illustrated in Fig. 9, which shows the temperature difference between two detectors positionned at $d/D = \pm 1$ for three values of T_{a} and a constant heater temperature $T_{\text{H}} = 393K$. These data were obtained via numerical simulation of the flow over a cylinder of diameter D, as presented in Sect. 2.

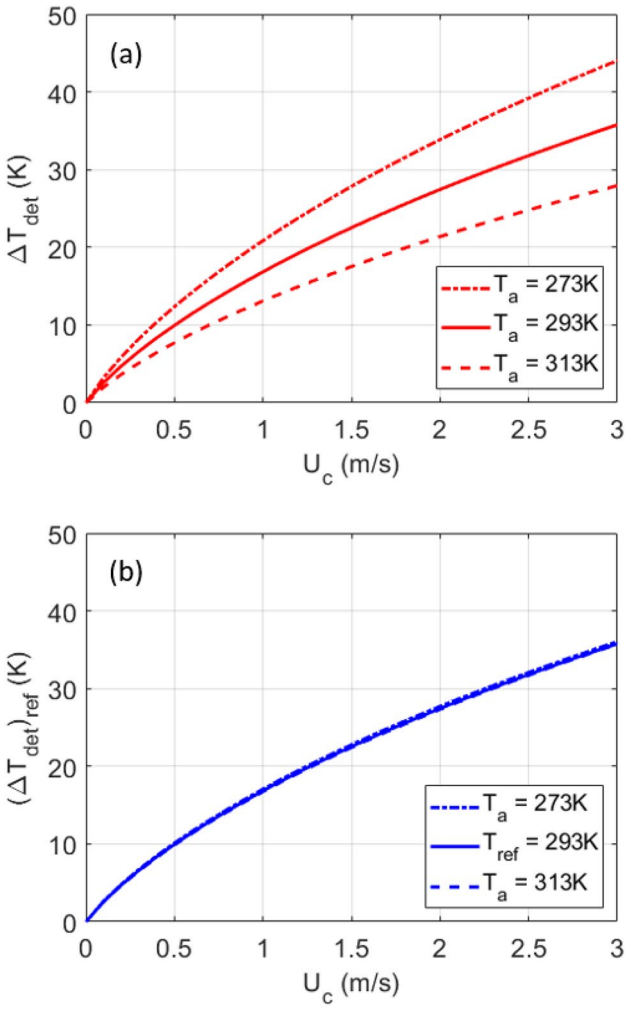

Fig. 9 Temperature difference ΔT_{det} between two detectors placed at $\pm d/D = 1$ accross a cylinder for three exemplary values of the air temperature T_{a} (**a**); Corrected temperature difference per Eq. 1 with $m = 1.05$ (**b**)

Although the simulated geometry is simpler than actual wall sensors, a similar effect is expected to occur in reality.

Figure 9(a) shows that the temperature difference ΔT_{det} between the two detectors varies as a function of T_{a}. When T_{a} is relatively large (i.e. closer to the heater temperature T_{H}), ΔT_{det} decreases compared to the reference case. Reciprocally, a smaller T_{a} implies a larger temperature difference ΔT_{det}. This behavior can be understood by examining the temperature profiles around the cylinder shown in Fig. 2(a): a smaller temperature span between T_{a} and T_{H} necessarily produces a smaller difference in temperature between the upstream and downstream sides of the heater. Thus, increasing T_{a} for a fixed value of T_{H} implies a decrease of the signal $E_{\text{det}} \propto \Delta T_{\text{det}}$.

In the field of hot-wire anemometry, several temperature correction methods have been proposed over the years (Bruun 1995; Hultmark and Smits 2010). Here, we suggest the empirical correction

$$(\Delta T_{\text{det}})_{\text{ref}} = \Delta T_{\text{det}} \left[\frac{T_{\text{H}} - T_{\text{ref}}}{T_{\text{H}} - T_{\text{a}}} \right]^{m}, \tag{1}$$

which, as may be seen in Fig. 9(b), properly collapses the simulated calibration curves. The exponent $m = 1.05 \simeq 1$ was chosen by trial and error and, in practical applications, might depend on the sensor geometry, wall shear stress, and temperature ranges under consideration. This correction merely necessitates the measurement of the air temperatures T_{ref} and T_{a} during calibration and measurements, respectively. In practice, an output voltage E_{det} measured at $T_{\text{a}} \neq T_{\text{ref}}$ may be corrected to $(E_{\text{det}})_{\text{ref}}$ by replacing ΔT by E in Eq. 1. A calibration law obtained at T_{ref} may then be used to obtain τ_w from $(E_{\text{det}})_{\text{ref}}$.

Finally, we now consider the dynamic behavior of the new calorimetric sensors. A priori, their frequency response is influenced by three separate parameters: (1) the capability of the heater to maintain a constant temperature in the presence of fluctuations of the wall shear stress, (2) the dynamic behavior of the local temperature field around the heater, and (3) the frequency response of the detectors that are operated with a constant current. As described in Sect. 3, the heater is maintained at a constant temperature using a CTA circuit. Its frequency response was estimated at 25 kHz by Weiss et al. (2017b) using a square-wave test, which implies that the heater is probably not the limiting factor in terms of overall frequency response. The dynamic behavior of the local flow around the heater and the frequency response of the detectors would be difficult to estimate without highly resolved numerical simulations. This is left to further endeavors. Here, our strategy is to estimate the frequency response of the calorimetric sensor though a comparison with a reference sensor with known dynamic behavior.

The selected reference sensor is a surface hot wire, the description of which is given by Sturzebecher et al. (2001). It consists of a 1.2 mm long tungsten wire of 5 µm in diameter that was installed flush to the wall over a 20 µm-deep groove. The wire was operated by a DISA 55M10 Constant Temperature Anemometer (CTA) at an overheat ratio of 0.7. The CTA was tuned using a square-wave test to reach a cut-off frequency of approximately 40 kHz (Bruun 1995; Weiss et al. 2001). Comparative tests were performed in the calibration facility at an average wall shear stress of 2 Pa, for which the flow is fully turbulent. This corresponds to a friction velocity of 1.3 m/s and a friction Reynolds number $\text{Re}_\tau = Hu_\tau/\nu \simeq 1300$, where $H = 15$ mm is the height of the calibration channel. We note that there is 20 % difference in length between the surface hot-wire ($l = 1.2$ mm, $l^+ = 102$) and the calorimetric sensor ($l = 1.0$ mm, $l^+ = 85$). Here l^+ is the physical length l of the sensors divided by the viscous

length scale ν/u_τ. According to the classical analysis of Wyngaard (1968), both sensors are too long to accurately characterize the smallest turbulent scales in this fully turbulent flow, though the effect of spatial averaging will be roughly equivalent for both sensors. On the other hand, given that the surface hot-wire has a high cut-off frequency, it is a relevant reference to test the overall frequency response of the calorimetric sensors. Finally, we note that the cavity depths of the calorimetric sensor and surface hot wire amount to 17 and 1.7 times the viscous length scale, respectively.

A comparison between the normalized power spectral densities (PSD) of the hot-wire signal and the calorimetric output E_{det} is shown in Fig. 10(a). It can be observed that the hot-wire PSD features a $f^{-5/3}$ decay that is characteristic of the inertial subrange up to approximately 10 kHz. The PSD of E_{det} follows the hot-wire signal up to approximately 2 kHz, after which it drops off precipitously. Taking the hot-wire signal as a reference, it is possible to estimate the frequency response of the calorimetric sensor by simply dividing the two PSDs and converting the results to decibels. This is done in Fig. 10(b), which shows a flat frequency response with a −3dB cut-off frequency of approximately 2.5 kHz for the calorimetric sensor. Furthermore, the decay of −20 dB/dec after the frequency roll-off is consistent with the first-order character of typical constant-current anemometers (Comte-Bellot 2007). This suggests that the overall frequency response of the calorimetric sensors is limited by the dynamic behavior of the detectors. Finally, we note that the frequency response obtained herein is consistent with that observed by Weiss et al. (2022) from the comparison of the PSD of E_{det} with that of a commercial capacitive shear stress sensor.

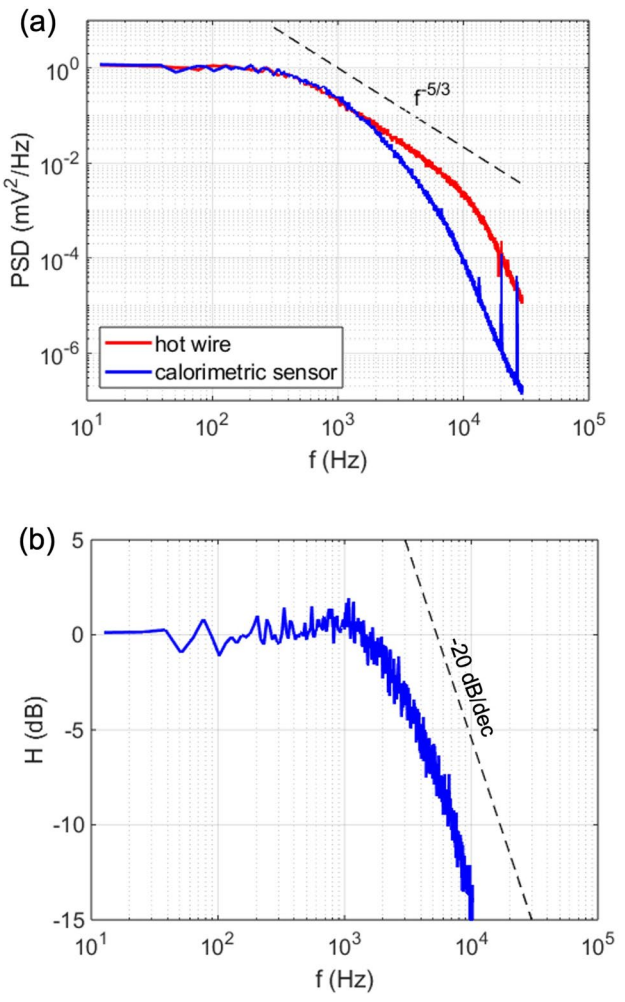

Fig. 10 Spectra of wall hot wire and calorimetric sensor output E_{det} in turbulent channel fow ($\tau_w = 2$ Pa) (**a**); Estimated transfer function of calorimetric sensor output (**b**)

In summary, the results presented in this section demonstrate that the new calorimetric sensors are capable of measuring the wall shear stress in direction and magnitude. Their range is approximately ±10 Pa and their frequency response is flat up to approximately 1 kHz. This makes the sensors well adapted to measurements in low-speed aerodynamic flows in the presence of boundary-layer separation. Furthermore, the sensors bear a certain resemblance to classical hot wires, with a non-linear response curve and a directional sensitivity close, but not equal to the cosine law. Therefore, these sensors are most useful when their axis is oriented parallel to the mean, near-wall flow. In the remainder of the article we will present a few examples of their application in low-speed, separating flows.

5 Applications

In the following, we present experimental results obtained with the sensors described above in three flow cases: a turbulent diffuser, a laminar separation bubble, and a low-Reynolds number airfoil.

5.1 Turbulent diffuser flow

Our first flow case is the turbulent separation bubble occuring on a one-sided diffuser. The experiments were carried out in a temperature-regulated, closed-loop wind tunnel at a nominal velocity $U_{\text{ref}} = 20$ m/s. The 600 mm wide test section is equiped with a backward-facing ramp on its floor, while the ceiling is kept flat at $y = 400$ mm above the upper ramp corner. As illustrated in Fig. 11, the ramp angle is $\alpha = 20°$ and the length of the inclined surface is $L_s = 340$ mm. The (x, y) coordinate system used in this study is aligned with the horizontal freestream velocity U_{ref}.

Upstream of the upper ramp corner, for $x < 0$, a turbulent boundary layer develops naturally on the test section floor

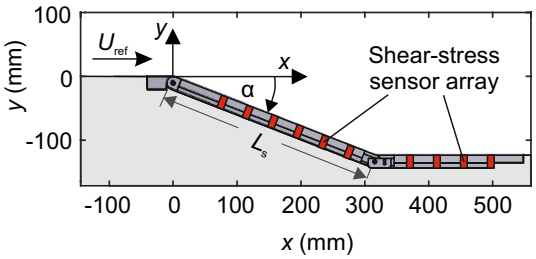

Fig. 11 Sketch of diffuser test section, $U_{ref} = 20$ m/s and is $\alpha = 20°$. Reproduced from Weiss et al. (2022) with permission

at conditions close to zero pressure gradient. Its Reynolds number based on momentum thickness just upstream of the ramp is $\mathrm{Re}_\theta = 5200$, with $\delta_{99} = 17$ mm and $\theta = 3.9$ mm. Downstream of the first corner, the boundary layer faces an adverse pressure gradient that leads to its separation from the surface. Then, reattachment occurs further dowstream due to the convex geometry of the test section. The main objective of the experiment was the investigation of the low-frequency dynamics of the turbulent separation bubble, as described in Weiss et al. (2022). Here, we concentrate on a few salient results obtained with the calorimetric sensors and expand the discussion on measurement uncertainty.

An array of 10 calorimetric sensors was used to measure the wall shear stress along the diffuser centerline ($z = 0$ mm), as indicated in Fig. 11. The sensors were installed flush to the test surface with their beams perpendicular to the diffuser symmetry axis. Previously performed oil-film visualizations indicated that the flow is symmetric with respect to the diffuser centerline (Weiss et al. 2022). Hence, the longitudinal shear stress was measured (i.e., $\phi = 0$ deg in Fig. 8). The 10 sensors were previously calibrated in the channel-flow facility discussed in Sect. 4.

Time histories of the wall shear stress at the 10 measurement stations are presented in Fig. 12. Those were recorded with a 16-bit data acquisition card for a total period of 180 s at a sampling rate of 5000 Hz. The main take-away of Fig. 12 is that the calorimetric sensors are indeed capable of measuring instantaneous backflow on the diffuser surface, as the signals oscillate between positive and negative values. At the most upstream position on the ramp (bottom of Fig. 12), the flow goes almost exclusively in the downstream direction ($\tau_w > 0$). The amplitude of the signal stays below $\tau_w = 1$ Pa most of the time, although several excursions up to $\tau_w \simeq 2$ Pa can be observed over the 180 s of recorded signal. While proceeding downstream, the amount of time featuring negative excursions of $\tau_w(t)$ increases, which indicates a larger proportion of backflow. Nevertheless, even near the bottom of the ramp (5th and 6th time traces), there are always instants of downstream-oriented near-wall flow with $\tau_w(t) > 0$. We also note that an examination of the PSDs in Weiss et al. (2022) revealed that most of the fuctuating

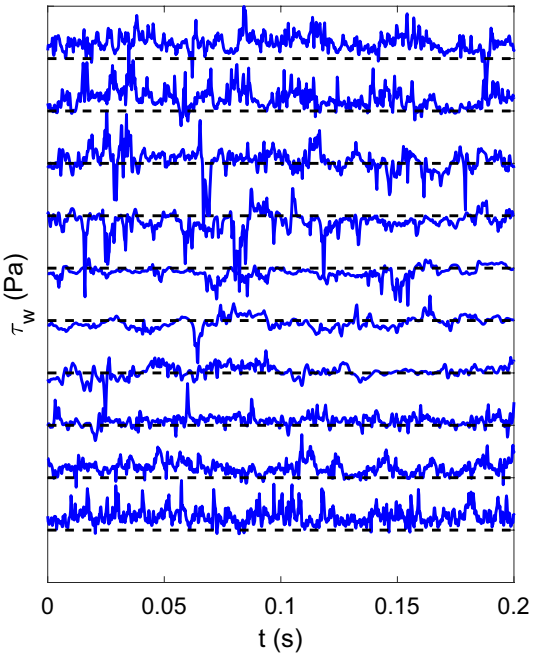

Fig. 12 Histories of wall shear stress $\tau_w(t)$ at the 10 sensor locations (x increasing from bottom to top); horizontal dashed lines: $\tau_w = 0$ Pa; vertical distance between dashed lines: 1 Pa

energy occurs at frequencies below 1 kHz, and this at all streamwise positions on the diffuser. This indicates that the bandwidth of the sensors is sufficient to capture the wall shear stress in this separated flow.

Streamwise distributions of the average and standard deviation of the wall shear stress are shown in Fig. 13, together with the forward-flow fraction on the right axis. Recall that the forward-flow fraction γ_u is defined as the

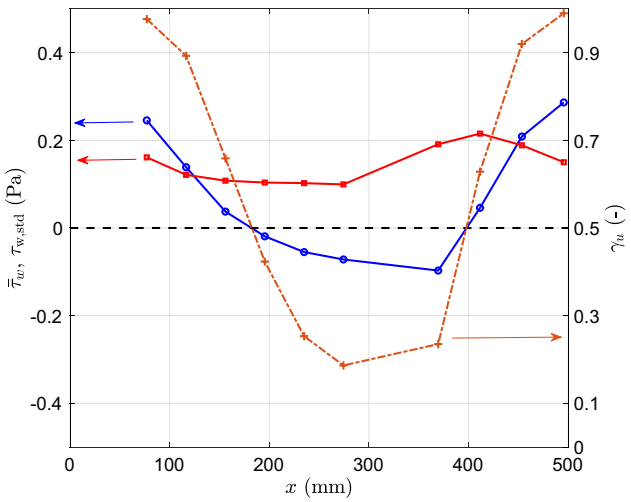

Fig. 13 Statistics of fluctuating wall shear stress along the diffuser centerline: mean (∘, left axis), standard deviation (□, left axis), and forward-flow fraction (+, right axis)

percentage of time that the flow goes in the positive x-direction (Simpson 1989). The average shear stress indicates a region of mean backflow ($\overline{\tau_w} < 0$) between $x = 200$ mm and $x = 400$ mm. The zero crossings of $\overline{\tau_w}$ coincide exactly with a forward-flow fraction $\gamma_u = 0.5$, which is an expected result (Simpson 1989). The distribution of $\tau'_{w,\mathrm{std}}$ indicates that the fluctuations decrease upstream of the mean separation point, stay relatively constant in the first half of the backflow region, and then increase again as the shear layer reattaches to the wall. This behavior is consistent with the shear-stress fluctuations measured by Spazzini et al. (1999) downstream of a backward-facing step with a double hot-wire wall probe. Interestingly, the standard deviation of the wall shear stress is of the same order of magnitude as its mean value. For reference, the measurements of Alfredsson et al. (1988), confirmed by the DNS of Örlü and Schlatter (2011), suggest a value of $\tau'_{\mathrm{std}}/\overline{\tau}_w \simeq 0.4$ for a zero-pressure-gradient turbulent boundary layer, which is not yet achieved at the most downstream measurement station. Finally, we note that the forward-flow fraction never reaches zero on the diffuser, which means that there is no position on the diffuser where the flow is reversed 100% of the time.

The results presented so far demonstrate the capability of calorimetric sensors to measure the mean and fluctuating wall shear stress in turbulent separated flows. At this stage, it is worth discussing the accuracy of the measurements. In previous work, we investigated the repeatability of calibration curves similar to Fig. 7 and found that they are repeatable within approximately 1% in laboratory conditions (Weiss et al. 2017b). Thus, in the diffuser experiment, the two main sources of uncertainty are a potential misalignment of the sensors with respect to the symmetry axis, and a possible temperature difference of one to two degrees between calibration in the channel flow facility and measurements in the (temperature-controlled) wind tunnel. From the numerical study of temperature effects shown in Fig. 9, we can estimate a variation $\Delta\tau_w/\tau_w$ of approximately $\pm 2\%$ per degree Celcius on the calibration curves (this was done by computing the effect of ΔT on the cooling velocity U_c and assuming that the latter is equivalent to the friction velocity $u_\tau = \sqrt{\tau_w/\rho}$). Hence, a difference of ± 2°C between calibration and measurements would lead to an uncertainty $\Delta\tau_w/\tau_w \sim \pm 4\%$. Further assuming that the sensor might be misaligned by up to $\pm 20°$ with respect to the ramp axis would add, according to Fig. 8, a $-10\%/0\%$ bracket to this estimate, thus leading to a total uncertainty of $\Delta\tau_w/\tau_w \sim -15\%/+5\%$. This level of uncertainty is consistent, though slightly larger, than the accuracy of $\pm 5\%$ that we previously quoted based on a comparison with a Preston tube, a hot-film probe, and an obstacle-wire sensor in a flat plate turbulent boundary layer (Weiss et al. 2017b). Finally, we note that the error sources that were just discussed do not apply to the measurement of the forward-flow fraction, since the sign switching between positive and negative shear stress is captured at any temperature and sensor alignment. Here, the main error source is an improper convergence of the statistical estimate. Given the relatively long measurement time of 180 s, we consider this uncertainty to be negligible in the present experiment.

5.2 Laminar separation bubble

Our second test case is a laminar separation bubble (LSB) that forms on a flat test surface by a combination of adverse and favorable pressure gradients. The experiments were performed in the TFT boundary layer wind tunnel described in Mohammed-Taifour et al. (2015). As shown in Fig. 14, this blow-down facility features a rectangular test section of 600 mm in width and 150 mm in height, in the first half of which a ZPG boundary layer develops on the upper test surface. The boundary layer then separates because of the diverging test-section floor and reattaches further downstream when the floor converges again. The wind tunnel was already used by Mohammed-Taifour and Weiss (2016) to study the unsteady behavior of a turbulent separation bubble. For the present experiments, the floor angles were modified and the velocity was reduced to $U_{\mathrm{ref}} = 4$ m/s to generate a large LSB on the upper test surface. Velocity measurements by Mohammed-Taifour et al. (2021) with a hot-wire probe revealed that the incoming boundary layer follows the Blasius profile in the upstream ZPG region of the test section. At $x = 1.2$ m, just upstream of the LSB, the boundary-layer thickness is $\delta = 10.7$ mm and the momentum thickness is $\theta = 1.4$ mm, thus resulting in a Reynolds number $\mathrm{Re}_\theta = 370$. The boundary layer then separates becauses of the APG, and laminar-turbulent transition occurs in the shear layer before it reattaches to the test surface. Dowstream of the LSB, a turbulent boundary layer develops in conditions close to ZPG. The length of the LSB was estimated at $L_{\mathrm{LSB}} \simeq 0.25$ m based on the meaasured boundary-layer profiles (Mohammed-Taifour et al. 2021). In the present experiments, calorimetric shear stress sensors were positioned on the test section centerline to measure the wall shear stress along the LSB. The main objective was to investigate if such sensors are sensitive enough to operate in regions of very low shear stress.

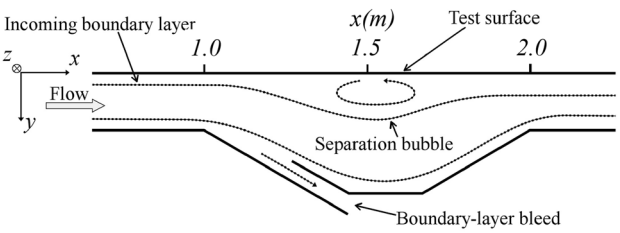

Fig. 14 Test section of the TFT boundary layer wind tunnel

The sensors' output voltage E_{det} was recorded using a 24-bit data acquisition card at a sampling rate of 2000 Hz.

Calibration of the sensors in the low-τ_w range was performed in two steps: first, the sensors were positioned in the ZPG laminar boundary layer well upstream of separation and their output voltage was recorded while the wind-tunnel velocity was increased step by step. The velocity was kept sufficiently low to maintain the laminar regime, so that the wall shear stress could be computed from the Blasius profile. In a second step, the sensors were positioned in the turbulent boundary layer downstream of the LSB, the velocity was increased, and the local wall shear stress was measured using a Preston tube. Following this experimental procedure, all data points were then fitted with a third-order polynomial function, as shown in Fig. 15 for an exemplary sensor. While there is some scatter between the points, the calibration curve demonstrates that the calorimetric sensors are very sensitive in the low-τ_w range. Hence, we estimate that the accuracy of this in-situ calibration procedure is within ± 0.01 Pa.

The streamwise distribution of the average and fluctuating wall shear stress, as well as the forward-flow fraction, are presented in Fig. 16. Starting with the latter (right axis), we notice that, in contrast to the turbulent case shown in Fig. 13, γ_u switches abruptly from one to zero between $x = 1.40$ m and $x = 1.45$ m. This is consistent with the usual picture of an LSB where the separation line is fixed in space and time (Gaster 1967), and contrary to TSBs where γ_u gradually decreases when the turbulent boundary layer lifts up from the surface (Simpson 1989; Mohammed-Taifour and Weiss 2016). The forward-flow fraction then stays equal to zero up to $x = 1.60$ m, which indicates a backflow region of approximately 0.1 m in length on the test surface. From

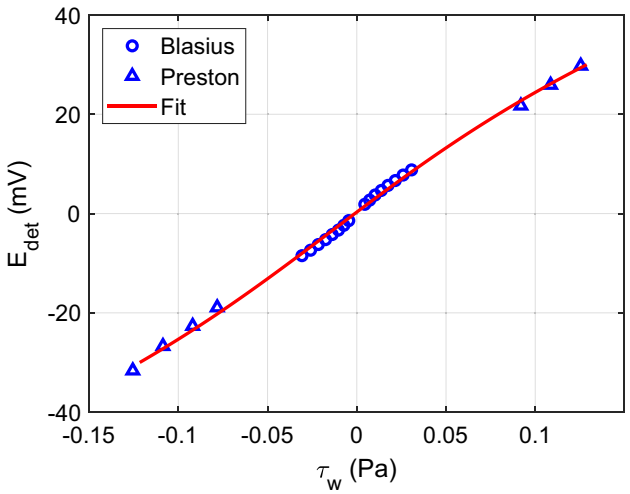

Fig. 15 In-situ calibration of a calorimetric sensor in the TFT boundary layer wind tunnel

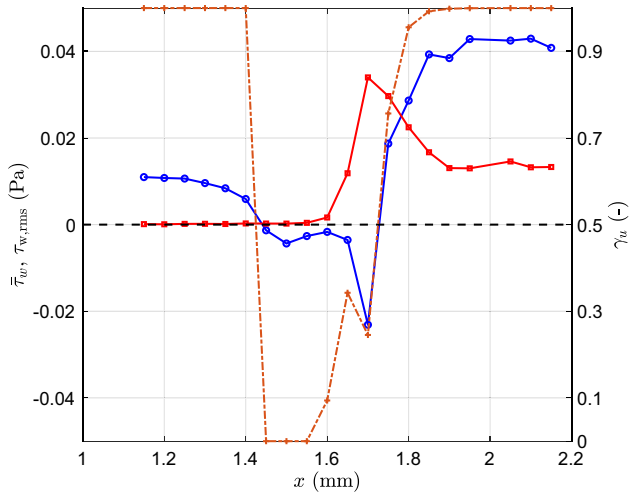

Fig. 16 Statistics of fluctuating wall shear stress along the LSB: mean (∘, left axis), standard deviation (□, left axis), and forward-flow fraction (+, right axis)

$x = 1.60$ m to $x = 1.85$ m, γ_u then gradually increases while the (turbulent) shear layer reattaches to the wall. Defining the length of the LSB as the distance between the two positions where $\gamma_u = 0.5$, we obtain a value $L_{\text{LSB}} \simeq 0.30$ m that is slightly larger than the estimate from hot-wire anemometry. Further dowstream, the forward-flow fraction stays close to one as the turbulent boundary layer develops on the test surface. Interestingly, we note that in the 180 s of recording period, γ_u is exactly 1.0 upstream, but approximately 0.9999 dowstream of the LSB. This might be caused by rare backflow events in the turbulent boundary layer, as described in Örlü and Vinuesa (2020), though more detailed experiments would be required to confirm this hypothesis. Overall, the distribution of γ_u is qualitatively consistent to that observed by Spalart and Strelets (2000) via Direct Numerical Simulation (DNS) of a flat-plate LSB at $\text{Re}_\theta \simeq 120$ (see their Fig. 4), though in the present case, reattachment probably occurs sooner because of the presence of a favorable pressure gradient.

The average wall shear stress $\overline{\tau_w}$ stays very low at all investigated positions (indeed, the left axis of Fig. 16 is an order of magnitude lower than in the TSB of Fig. 13). The first zero crossing of $\overline{\tau_w}$ occurs between $x = 1.40$ m and $x = 1.45$ m, exactly where γ_u switches from 1 to 0. The wall shear stress then stays roughly constant until $x = 1.65$ m before a negative peak occurs at $x = 1.70$ m. This peaks corresponds to the maximum of $\tau'_{w,\text{std}}$ and to a small dip in the distribution of γ_u, and is attributed to the spanwise vortices that develop in the shear layer in the early stages of transition. The minimum of $\overline{\tau_w}$ corresponds to a friction coefficient $c_f = \overline{\tau_w}/(\frac{1}{2}\rho U_{\text{ref}}^2) = -0.0024$, which is in good agreement with the DNS results of Spalart and Strelets (2000) and Alam and Sandham (2000). Following this

negative peak, $\overline{\tau_w}$ increases abruptly, crosses zero again when the shear layer reattaches, and settles to a value of $\overline{\tau_w} \simeq 0.04$ Pa downstream of the LSB. Here again, the qualitative distribution of the average wall shear stress is fully consistent with existing DNS results (Spalart and Strelets 2000; Alam and Sandham 2000).

Finally, the standard deviation $\tau'_{w,\mathrm{std}}$ stays very low upstream of separation and in the first half of the LSB, where the flow is still laminar. There, the signal is very close to the noise floor of the calorimetric sensor, whose standard deviation is approximately 0.001 Pa. It then increases steeply until a maximum is reached at a position just upstream of the mean reattachment ($x = 1.70$ m). There, as can be observed in Fig. 17, the signal is characterized by strong quasi-periodic negative fluctuations suggesting the passsage of spanwise rollers typically seen in the early stages of transition in LSBs [e.g., Lambert and Yarusevych (2017)].

In summary, the results presented in this section demonstrate that the calorimetric sensors are capable of measuring the very low shear stress that typically occur in low-speed, laminar flows. Furthermore, their bi-directionality is well adapted to the measurement of laminar separation and laminar/turbulent transition. Incidentally, the results presented herein are a welcome addition to a scarce experimental database of wall shear stress in LSBs.

5.3 NACA 0015 airfoil

Our final test case is the flow over the suction side of a NACA 0015 airfoil at relatively low Reynolds number. For those experiments, an array of 10 calorimetric microsensors was mounted on a semi-flexible printed circuit board (PCB) that was fixed on the pressure side of a two-dimensional wing model made of wood. Figure 18 shows an image of the model installed in the test section of a blow-down wind tunnel. The chord length of the wing is $c = 0.2$ m and the test-section dimensions are 0.4 m × 0.4 m. The sensors cover a streamwise distance $x/c = 0.27 - 0.67$. They were previously calibrated by installing the complete PCB in the channel-flow facility described in Sect. 4 (Schwarz 2023). Unfortunately, the seventh sensor in the array failed during calibration and is not included in the figures below. The reference velocity in the wind tunnel was set to 15 m/s, which resulted in a chord Reynolds number of $\mathrm{Re_c} = 2 \times 10^5$.

Figure 19 shows the streamwise distribution of the average wall shear stress $\overline{\tau_w}$ for selected values of the airfoil angle of attack α. At low angles of attack ($\alpha = 0°$ and $\alpha = 3°$), $\overline{\tau_w}$ increases, reaches a maximum, and decreases again. This is indicative of laminar-turbulent transition occurring over the length of the sensor array, which was confirmed by the absence of such a distribution when a transition trip was

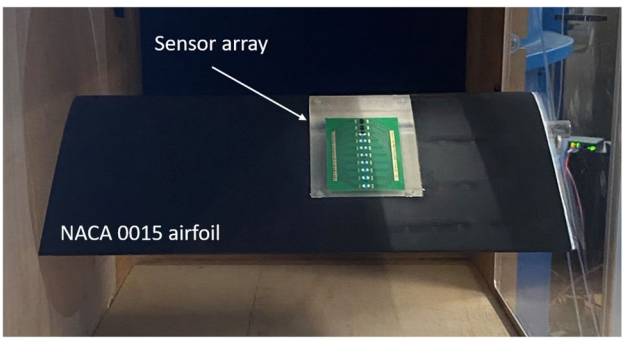

Fig. 18 Wind-tunnel test section with NACA 0015 airfoil and array of calorimetric sensors

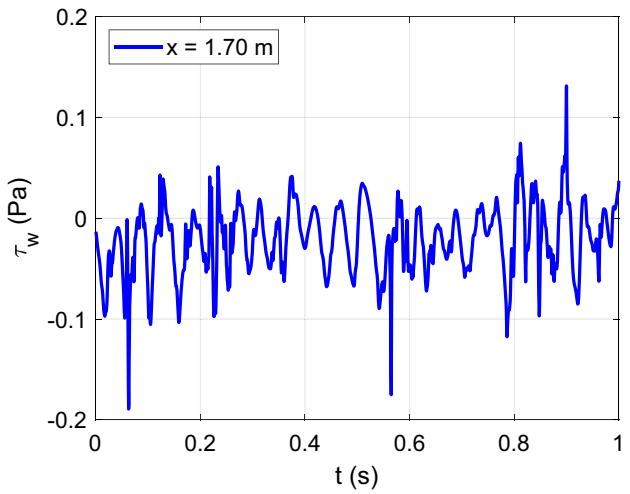

Fig. 17 Time trace of fluctuating wall shear stress at $x = 1.70$ m

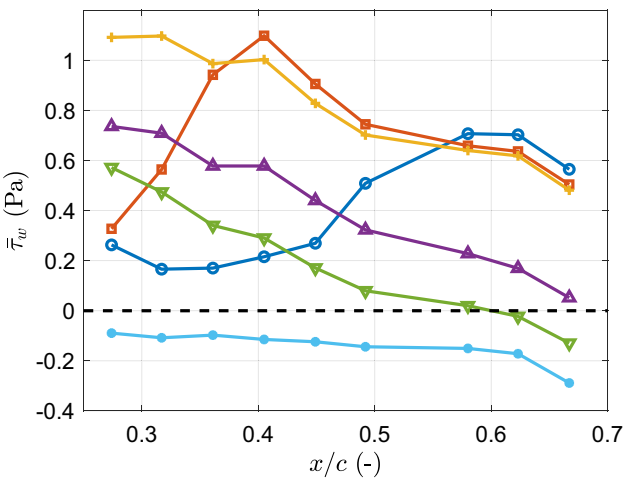

Fig. 19 Distribution of average wall shear stress over NACA 0015 airfoil for $\alpha = 0°$ (○), $\alpha = 3°$ (□), $\alpha = 5°$ (+), $\alpha = 10°$ (△), $\alpha = 12°$ (▽), and $\alpha = 14°$ (∗)

placed near the airfoil leading edge (not shown here). At higher angles of attack, the streamwise distribution of $\overline{\tau_w}$ monotonously decreases as a turbulent boundary layer flows over the sensors. Increasing the angle of attack reduces the amplitude of the wall shear stress as the boundary layer faces an ever-increasing adverse pressure gradient. At $\alpha = 12°$, the two most downstream sensors indicate a negative shear stress, which shows that the flow is already separated in the mean at $x/c \simeq 0.6$. Finally, at $\alpha = 14°$, the separation line has moved close to the leading edge and the flow over the sensor array is completely separated, as indicated by the low negative values of $\overline{\tau_w}$. Overall, the distributions of $\overline{\tau_w}$ are consistent with the expected aerodynamic behavior of a NACA 0015 airfoil operating at relatively low Reynolds number (Winslow et al. 2018).

Deeper understanding of the flow physics in the boundary layer can be obtained by considering the streamwise distribution of forward-flow fraction γ_u in Fig. 20. Here, γ_u is close to 1 over all sensors at $\alpha = 0°$ and $\alpha = 5°$. On the other hand, for $\alpha = 3°$, a significant amount of instantaneous backflow can be observed on the first two sensors. This suggests that, for low angles of attack, transition on the NACA 0015 occurs within a LSB, which, again, is consistent with existing knowledge (Winslow et al. 2018). Interestingly, no such LSB occurs at $\alpha = 0°$ since the transition process is associated with a forward-flow fraction of 1. This is presumably because of the absence of a strong adverse pressure gradient at zero angle of attack. At $\alpha = 5°$ and higher, we suppose that the LSB has simply moved upstream of the instrumented area, and that the turbulent flow is attached over the sensor array. For higher angles of attack, regions of instantaneous backflow are now measured by the downstream sensors, which suggests that they are linked to turbulent separation slowly progressing upstream of the trailing edge as α is increased. In a manner consistent with the average wall shear stress, the forward-flow fraction is very low over the complete sensor array at $\alpha = 14°$, indicating a fully separated flow. These results further demonstrate that, in order to accurately measure the wall shear stress on an airfoil, sensors capable of capturing regions of instantaneous backflow are required.

Finally, we compare in Fig. 21 the distribution of the average wall shear stress $\overline{\tau_w}$ measured by the calorimetric shear stress sensors at $\alpha = 3°$ with that computed by the XFLR5 aerodynamic analysis software. For the latter, the position of laminar-turbulent transition was set to $x/c = 0.28$ by trial and error. This was required since the exact transition process is known to be extremely sensitive to the experimental set up (Boiko et al. 2002). Nevertheless, the values of $\overline{\tau_w}$ calculated by XFLR5 in both the transitional and turbulent regimes match the measured values very well, thus validating the proposed experimental method.

6 Conclusion

This article introduced new MEMS calorimetric sensors for the measurement of wall shear stress in low-speed aerodynamic flows. The sensors are made of three beams of platinum-plated silicon nitride suspended over a small cavity. The middle beam acts as a heater and the two side beams as wake detectors. Combined with a proper analog circuitry, the sensors output a voltage that is a function of the wall shear stress just upstream of the cavity. Calibration in several facilities demonstrated that the sensors have a range and bandwidth of the order of ±10 Pa and 1 kHz,

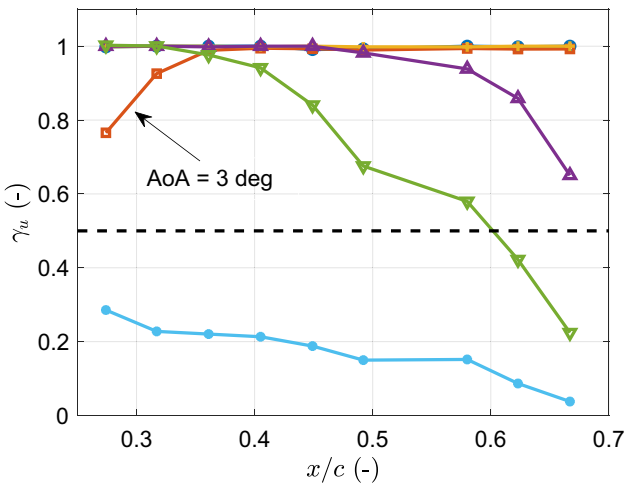

Fig. 20 Distribution of forward-flow fraction over NACA 0015 airfoil for $\alpha = 0°$ (○), $\alpha = 3°$ (□), $\alpha = 5°$ (+), $\alpha = 10°$ (△), $\alpha = 12°$ (▽), and $\alpha = 14°$ (∗)

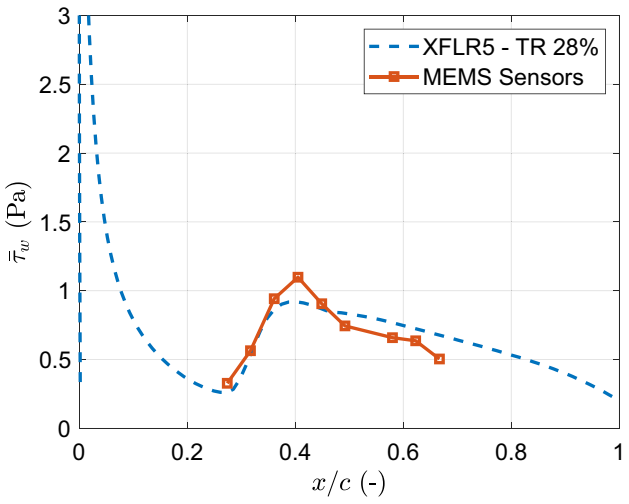

Fig. 21 Comparison between measured wall shear stress and calculation with XFLR5 for $\alpha = 3°$

respectively. Their angular response and temperature sensitivity make them relatively similar to near-wall hot wires, but with the added advantage of sensitivity to flow direction. As such, the new calorimetric shear-stress microsensors are well adapted to the measurement of separating and reattaching flows.

Application examples included the flow in a laminar separation bubble, a turbulent separation bubble, and on a low-Reynolds-number airfoil. In all cases the capacity of the sensors to measure instantaneous backflow was demonstrated. Hence, both the mean and fluctuating wall shear stress can be measured. This allows the determination of relevant statistics like the forward-flow fraction or various statistical moments of the wall shear stress in laminar, transitional, or turbulent separating and reattaching flows.

While our sensors clearly offer new possibilities to the aerodynamicist, further improvements are possible:

- The inter-beam distance d between heater and detectors has been shown to be the main parameter driving the sensor's range. Decreasing its value below its current standard of $d = 5\,\mu\text{m}$ would lead to further improvements in the amplitude of wall shear stress that can be detected.
- In the same spirit, drastically decreasing the overall sensor's dimension, in a manner similar to the nanoscale hot-wire of Bailey et al. (2010), may lead to significant improvements in spatial and temporal resolution that could allow for a detailed investigation of wall-shear-stress fluctuations in fully turbulent flows.
- Finally, one may want to advantageously use the sensor's angular sensitivity by designing novel two-dimensional calorimetric sensors that, after a proper calibration, would capture the instantaneous shear-stress vector on the wall.

We hope that the experimental results presented in this article will encourage researchers to pursue these ideas.

Acknowledgements The development of the MEMS calorimetric sensors described in this article benefited from the help of many students and colleagues. For the results shown herein, we are especially indebted to Alex Gothow, Ben Steinfurth, Simon Schwarz, and Killian Zimmer from Technische Universität Berlin, to Léo Chamard and Philippe Combette from Université de Montpellier, and to Abdelouahab Mohammed-Taifour, Théo Quirion, and Marlène Sanjosé from École de technologie supérieure in Montréal.

Funding Open Access funding enabled and organized by Projekt DEAL. Not applicable.

Data availability Not applicable.

Declarations

Ethical approval Not applicable.

Open Access This article is licensed under a Creative Commons Attribution 4.0 International License, which permits use, sharing, adaptation, distribution and reproduction in any medium or format, as long as you give appropriate credit to the original author(s) and the source, provide a link to the Creative Commons licence, and indicate if changes were made. The images or other third party material in this article are included in the article's Creative Commons licence, unless indicated otherwise in a credit line to the material. If material is not included in the article's Creative Commons licence and your intended use is not permitted by statutory regulation or exceeds the permitted use, you will need to obtain permission directly from the copyright holder. To view a copy of this licence, visit http://creativecommons.org/licenses/by/4.0/.

References

Alam M, Sandham ND (2000) Direct numerical simulation of 'short'laminar separation bubbles with turbulent reattachment. J Fluid Mech 410:1–28

Alfredsson PH, Johansson AV, Haritonidis JH et al (1988) The fluctuating wall-shear stress and the velocity field in the viscous sublayer. Phys Fluids 31(5):1026–1033. https://doi.org/10.1063/1.866783

Bailey SCC, Kunkel GJ, Hultmark M et al (2010) Turbulence measurements using a nanoscale thermal anemometry probe. J Fluid Mech 663:160–179

Bailly C, Comte-Bellot G (2015) Turbulence. Springer

Boiko AV (2002) The origin of turbulence in near-wall flows. Springer

Bruun HH (1995) Hot-wire anemometry: principles and signal analysis. Oxford University Press

Castro I, Haque A (1987) The structure of a turbulent shear layer bounding a separation region. J Fluid Mech 179:439–468

Chamard L (2022) Étude et réalisation d'un microcapteur de contraintes de frottement pariétal á fonctionnement calorimétrique. PhD thesis, Université de Montpellier

Chamard L, Giehler J, Weiss J, et al. (2023) Simulation and testing of a family of calorimetric wall shear stress microsensors. IEEE Sensors J

Champagne FH, Sleicher CA, Wehrmann OH (1967) Turbulence measurements with inclined hot-wires part 1. Heat transfer experiments with inclined hot-wire. J Fluid Mech 28(1):153–175

Chandrasekharan V, Sells J, Meloy J et al (2011) A microscale differential capacitive direct wall-shear-stress sensor. J Microelectromech Syst 20(3):622–635

Comte-Bellot G (2007) Thermal anemometry. In: Tropea C, Yarin AL, Foss JF (eds) Handbook of experimental fluid mechanics. Springer, Berlin, pp 229–283

De Luca A, Haneef I, Coull JD et al (2015) High-sensitivity single thermopile SOI CMOS MEMS thermal wall shear stress sensor. Sensors J IEEE 15(10):5561–5568

Driver DM (2003) Application of oil-film interferometry skin-friction measurement to large wind tunnels. Exp Fluids 34:717–725

Elwenspoek M, Wiegerink R (2001) Mechanical microsensors. Springer

Fernholz H, Janke G, Schober M et al (1996) New developments and applications of skin-friction measuring techniques. Meas Sci Technol 7(10):1396

Gaster M (1967) The structure and behavior of laminar separation bubbles. Aeronautical Research Council Reports and Memoranda No. 3595

Ghouila-Houri C, Gallas Q, Garnier E et al (2017) High temperature gradient calorimetric wall shear stress micro-sensor for flow separation detection. Sensors Actuators A Phys 266:232–241

Ghouila-Houri C, Talbi A, Viard R et al (2019) Unsteady flows measurements using a calorimetric wall shear stress micro-sensor. Exp Fluids 60:1–10
Giehler J, Chamard L, Ebert C et al (2022) Surrogate-based parameter exploration for the design of MEMS calorimetric wall shear stress sensors by means of CFD. Sensors Actuators A Phys 347(113):949
Große S, Schröder W (2008) Mean wall-shear stress measurements using the micro-pillar shear-stress sensor MPS3. Meas Sci Technol 19(1):015403
Haritonidis JH (1989) The measurement of wall shear stress. In: Advances in fluid mechanics measurements. Springer, pp 229–261
Hultmark M, Smits AJ (2010) Temperature corrections for constant temperature and constant current hot-wire anemometers. Meas Sci Technol 21(10):105404
Kuo JT, Yu L, Meng E (2012) Micromachined thermal flow sensors-a review. Micromachines 3(3):550–573
Lambert AR, Yarusevych S (2017) Characterization of vortex dynamics in a laminar separation bubble. AIAA J 55(8):2664–2675
Lammerink TSJ, Tas NR, Elwenspoek M et al (1993) Micro-liquid flow sensor. Sensors Actuators A Phys 37:45–50
Mailly F, Giani A, Martinez A et al (2003) Micromachined thermal accelerometer. Sensors Actuators A Phys 103(3):359–363
Meritt RJ, Schetz JA (2016) Skin friction sensor development, validation, and application for high-speed, high-enthalpy flow conditions. J Propuls Power 32(4):821–833
Mohammed-Taifour A, Weiss J (2016) Unsteadiness in a large turbulent separation bubble. J Fluid Mech 799:383–412
Mohammed-Taifour A, Weiss J (2021) Periodic forcing of a large turbulent separation bubble. J Fluid Mech 915:A24
Mohammed-Taifour A, Schwaab Q, Pioton J et al (2015) A new wind tunnel for the study of pressure-induced separating and reattaching flows. Aeronaut J 119(1211):91–108
Mohammed-Taifour A, Sanjosé M, Weiss J (2021) Unsteadiness in a pressure-induced laminar separation bubble. In: Proceedings of 13th international ERCOFTAC symposium on engineering, turbulence, modeling and measurements (ETMM13), p 159
Örlü R, Schlatter P (2011) On the fluctuating wall-shear stress in zero pressure-gradient turbulent boundary layer flows. Phys Fluids 23(2):021704
Örlü R, Vinuesa R (2020) Instantaneous wall-shear-stress measurements: advances and application to near-wall extreme events. Meas Sci Technol 31(11):112001
Pabon RJ, Ukeiley L, Sheplak M et al (2018) Characteristics of turbulent boundary layer large scale motions using direct fluctuating wall shear stress measurements. Phys Rev Fluids 3(11):114604
Sabaté N, Santander J, Fonseca L et al (2004) Multi-range silicon micromachined flow sensor. Sensors Actuators A Phys 110(1):282–288
Schwaab Q, Weiss J (2015) Evaluation of a thermal-tuft probe for turbulent separating and reattaching flows. ASME J Fluids Eng 137(011401):1–7
Schwarz S (2023) Wall shear-stress measurements on an airfoil using calorimetric shear-stress sensors. Master's thesis, TU Berlin
Sheplak M, Spina EF, McGinley CB (1996) Progress in hot-film anemometry for hypersonic flow. Exp Therm Fluid Sci 13(1):21–28
Simpson RL (1989) Turbulent boundary-layer separation. Ann Rev Fluid Mech 21(1):205–232
Spalart PR, Strelets MK (2000) Mechanisms of transition and heat transfer in a separation bubble. J Fluid Mech 403:329–349
Spazzini P, Iuso G, Onorato M et al (1999) Design, test and validation of a probe for time-resolved measurement of skin friction. Meas Sci Technol 10(7):631–9
Steinfurth B, Weiss J (2022) Efficiency enhancement in active separation control through optimizing the duty cycle of pulsed jets. AIAA J 60(12):6566–6580
Steinfurth B, Weiss J (2022) modeling the decay of finite-span starting and stopping wall jets in an external stream. J Fluid Mech 951:A28
Sturzebecher D, Anders S, Nitsche W (2001) The surface hot wire as a means of measuring mean and fluctuating wall shear stress. Exp Fluids 31(3):294–301
Tobak M, Peake DJ (1982) Topology of three-dimensional separated flows. Ann Rev Fluid Mech 14(1):61–85
Weiss J, Knauss H, Wagner S (2001) Method for the determination of frequency response and signal to noise ratio for constant-temperature hot-wire anemometers. Rev Sci Instrum 72(3):1904–1909
Weiss J, Schwaab Q, Boucetta Y et al (2017) Simulation and testing of a MEMS calorimetric shear-stress sensor. Sensors Actuators A Phys 253:210–217
Weiss J, Jondeau E, Giani A et al (2017) Static and dynamic calibration of a MEMS calorimetric shear-stress sensor. Sensors Actuators A Phys 265:211–216
Weiss J, Steinfurth B, Chamard L et al (2022) Spectral proper orthogonal decomposition of unsteady wall shear stress under a turbulent separation bubble. AIAA J 60(4):2150–2159
Winslow J, Otsuka H, Govindarajan B et al (2018) Basic understanding of airfoil characteristics at low Reynolds numbers (10 4–10 5). J Aircr 55(3):1050–1061
Winter K (1977) An outline of the techniques available for the measurement of skin friction in turbulent boundary layers. Prog Aerosp Sci 18:1–57
Wyngaard JC (1968) Measurement of small-scale turbulence structure with hot wires. J Phys E Sci Instrum 1(11):1105

Publisher's Note Springer Nature remains neutral with regard to jurisdictional claims in published maps and institutional affiliations.